JOM
https://doi.org/10.1007/s11837-023-05751-4

Effect of Size, Location, and Aspect Ratio of Internal Pores on Failure Behavior of Laser Powder Bed Fusion Ti-6Al-4V

ERIK FURTON,[1] SELDA NAYIR,[1] and ALLISON M. BEESE [1,2,3]

1.—Department of Materials Science and Engineering, Pennsylvania State University, University Park, PA 16802, USA. 2.—Department of Mechanical Engineering, Pennsylvania State University, University Park, PA 16802, USA. 3.—e-mail: beese@matse.psu.edu

Notched tension Ti-6Al-4V samples were fabricated using laser powder bed fusion additive manufacturing. During the fabrication of each sample, a single internal pore was included, and its size, aspect ratio, and location were varied. The presence of pores significantly reduced the ductility of the samples, where the size and location of the pores were the most critical factors, in that order, and the aspect ratio was not impactful. The severity of the internal pore was quantified with the J-integral, revealing that fracture occurred at a critical value of 23 kN/m. Ductile fracture models were calibrated with the experimentally measured displacements to failure and used to quantify the location-dependent rate of damage accumulation. Although damage initiated near the surface (meaning that near-surface pores were critical in early deformation), the increased stress triaxiality at the center of the sample led to higher damage accumulation with respect to applied displacement for centrally-located pores.

INTRODUCTION

Ti-6Al-4V is one of the most commonly used alloys in laser powder bed fusion (L-PBF), because of its strength (1100–1400 MPa), ductility (2.8–10.4% in uniaxial tension), fracture toughness, and corrosion resistance.[1] Although additive manufacturing (AM) methods provide design flexibility, the adoption of AM for structural applications is limited due to variability in mechanical behavior.[2,3] Potential biomedical and aerospace applications require both high performance and reliability because of the large associated cost of failure.[4,5] The necessity to quantify and reduce risk in these fields has caused researchers, industry, and standards organizations to work together to develop process control, qualification, and inspection standards.[6]

One of the major contributing factors to the variability in mechanical properties is the presence of pores, which stochastically vary in size, shape, and location.[7–9] Components fabricated by AM can contain pores due to gas-entrapment, keyhole collapse (present with high energy densities), and lack-of-fusion (LOF, present with low energy densities).[10–13] Although post processing methods, such as hot isostatic pressing (HIP), have been applied to close defects, the pores are not completely healed and may reopen during subsequent loading.[14] Because of the challenge of eliminating pores in AM, the ASTM standard for AM terminology allows "fully dense" samples to contain micron-sized pores.[15]

Studies have shown that largely round keyhole pores can reduce strength; however, the sharp morphological features of LOF pores are more critical as they result in higher stress concentrations.[16,17] To quantify the effect of pores on properties, two approaches have generally been taken: either stochastically distributed pores are produced by using non-optimal processing parameters, resulting in measurements of processing-dependent properties, or a single internal pore is intentionally introduced by not melting powder at that location to isolate the effect of a single defect on mechanical behavior.[18–22] Meng et al. studied individual embedded spherical pores up to 2.8% of the cross-sectional area, and located in the center of the sample or near

Erik Furton and Selda Nayir have contributed equally to this work.

(Received December 5, 2022; accepted February 20, 2023)

Published online: 20 March 2023

the surface, in Ti-6Al-4V under uniaxial tension, and reported minimal effect on the failure behavior compared with fully dense samples.[23] Small cylindrical flaws (less than 0.5% of the cross-sectional area) in uniaxial tension samples were also found to be non-critical in the work of Furton et al.[20] However, under larger stress triaxialities, the presence of even a small pore (less than 0.5% of the cross-sectional area) drastically reduced both strength and ductility. A study interrogating how a pore's size, location, and aspect ratio affect fracture behavior at high stress triaxialities for monotonic loading has not yet been reported.

The rate of damage accumulation is known to be dependent on the stress state.[24–28] The stress state may be quantified by the stress triaxiality, η, and the normalized Lode angle parameter, $\overline{\theta}$. The stress triaxiality is defined as:

$$\eta = \frac{\sigma_m}{\sigma_{vM}}, \text{ where} \tag{1}$$

$$\sigma_{vM} = \sqrt{3J_2} \text{ with } J_2 = \frac{1}{2}\mathbf{s} : \mathbf{s},\ \boldsymbol{s} = \boldsymbol{\sigma} - \sigma_m \boldsymbol{I}, \text{ and } \sigma_m = \frac{tr(\boldsymbol{\sigma})}{3} \tag{2}$$

where σ_{vM} is the von Mises stress, J_2 the second invariant of the deviatoric stress tensor, $\boldsymbol{s}$, $\boldsymbol{\sigma}$ is the Cauchy stress tensor, and σ_m the mean stress. The normalized Lode angle parameter quantifies the relationship between the intermediate principal stress and the maximum and minimum principal stresses, and is given by:

$$\overline{\theta} = 1 - \frac{2}{\pi}\cos^{-1}\left(\frac{3\sqrt{3} \times J_3}{2 \times J_2^{3/2}}\right), \text{ where } J_3 = \det(\boldsymbol{s}) \tag{3}$$

The normalized Lode angle parameter ranges between –1 and + 1, and for a given value of stress triaxiality, a value of $\overline{\theta}$ near zero causes the most severe damage accumulation.[24] Increased stress triaxiality increases the microvoid growth rate with respect to plastic strain, thereby exponentially decreasing ductility for a given $\overline{\theta}$.[29] Notched tension samples are designed to probe the effect of stress triaxiality on fracture behavior at a constant $\overline{\theta} = 1$ at the sample's center, where a sharper notch results in higher stress triaxiality.[30]

Ductile fracture models quantify the effect of stress state on damage accumulation and fracture, and require calibration from mechanical tests conducted on samples that probe a wide range of stress states. During mechanical tests required for calibration, only surface deformations and applied loads are directly measured, while the stress state and accumulated plastic strain inside the sample are obtained from corresponding finite element simulations. For fracture quantification of pore-containing materials, an engineering approach has been used for ductile fracture models, where pores are not modeled in the finite element model;[31] rather, a fully dense finite element model is terminated at the experimentally measured displacement to failure of the pore-containing sample to determine the effective allowable strain to failure. Thus, instead of accounting for the increased local stresses and strains around the crack tip, the sample's allowable strength is reduced. Such an engineering approach has two primary benefits compared with modeling the defect. First, rather than requiring numerous simulations for various defect locations, orientations, and shapes, each material point accumulates damage as if it were weakened by a pore or crack. The most critical location may be identified by the element that accumulates the most damage. Second, a coarser mesh may be used because fine elements required to model a crack tip singularity are not required, and computational speed is therefore increased. The primary drawback of this engineering approach is that the physical significance of the fracture model's calibration parameters may be difficult to identify.

Increased understanding of failure behavior may be obtained by studying the J-integral, or crack driving force, defined as the rate of change of a sample's strain energy with respect to a crack's surface area.[32] The J-integral fully characterizes the strain distribution around a crack tip for an elastoplastic material without full-ligament yielding under monotonic loading.[33] To measure the critical J-integral at failure (J_f, as a material property), fracture toughness specimens have been developed, such as the compact tension (CT) and single edge-notch tension (SENT) geometries, with a surface crack under predominantly plane strain conditions.[32] However, J_f obtained from fracture toughness tests may not be directly applicable for flaw characterization in additively manufactured materials, because the pores are not necessarily atomically sharp, nor is the crack front necessarily under plane strain. Pore-containing notched tension samples, which fracture with limited ligament yielding due to high stress triaxiality, provide information about the critical J-integral that may be more representative of additively manufactured components in service, where pores are neither pre-cracked nor are exclusively subject to plane strain conditions.

In this study, notched tension Ti-6Al-4V samples were produced with L-PBF, and each sample contained a single designed internal pore at the minimum cross-section. To assess the impact of a single pore's location, the defects were designed to be located at the center of the sample, near the sample surface, or halfway between the sample center and surface. The diameters of the pores were varied from 0.12% of the cross-sectional area (212 μm equivalent diameter) and 0.25% of the cross-sectional area (300 μm equivalent diameter).

Pores had either circular or elliptical cross-sections, with aspect ratios of 1.0, 0.5, and 0.25. J-integrals for the various pore configurations were simulated with finite element models, and a critical value at fracture was identified. A ductile fracture model was calibrated with the samples containing circular pores. Both the J-integral analysis and the ductile fracture models highlight that pore location, in addition to pore size, significantly affect fracture behavior.

EXPERIMENTAL METHODS

Specimen Fabrication

All samples were fabricated with a ProX DMP 320 L-PBF machine (3D Systems, Rock Hill, SC) in which the oxygen concentration was kept below 20 ppm. The powder was gas atomized Grade 5 powder provided by 3D Systems with diameters ranging from 15 μm to 45 μm. Samples were fabricated using a laser power of 250 W, a scan speed of 1300 mm/s, a layer thickness of 60 μm, and hatch spacing of 80 μm. All of the samples were stress relieved in a vacuum furnace by holding below 10^{-3} Torr at 593 ± 13°C for 2 h and cooled in an argon atmosphere with 99.997% purity (Solar Atmospheres, Souderton, PA).

The samples were fabricated as cylinders, and then machined with a computer numerical control (CNC) lathe to the notched tension geometries shown in Fig. 1. The notch's machined surface finish decreased the likelihood of fracture initiating due to surface roughness effects. Two notch radii were fabricated: 3 mm (R3NT) and 5 mm (R5NT), which correspond to approximate stress triaxialities of 0.8 and 1.0, respectively. Each sample was designed to be fully dense, with the exception of a single elliptical pore, which was incorporated by interrupting the laser powder to mimic lack-of-fusion porosity. The pores were located at the critical cross-section, where the cross-sectional area was the smallest.

A full factorial experimental design was conducted, where the pore size, aspect ratio, and location were varied. To probe the effect of defect size, the test specimens' pores were designed to have equivalent diameters of 0.5% and 1.0% of the sample's cross-sectional area. The pores' cross-sections were designed to be either circular or elliptical, with aspect ratios varying from 1.00 to 0.50 to 0.25 (Fig. 2a). The equivalent diameter was kept constant, e.g., for an aspect ratio of 0.25, the major diameter of the pore was twice that of an equivalent-sized circular pore, while the minor diameter was half. The location of the pore was designed such that its center was either at the sample's center, 1.5 mm from the center, or near the sample's surface, where the center was one major axis away from the free edge (Fig. 2b). Elliptical pores were oriented such that their major axis was colinear with the sample's diameter. The designed internal

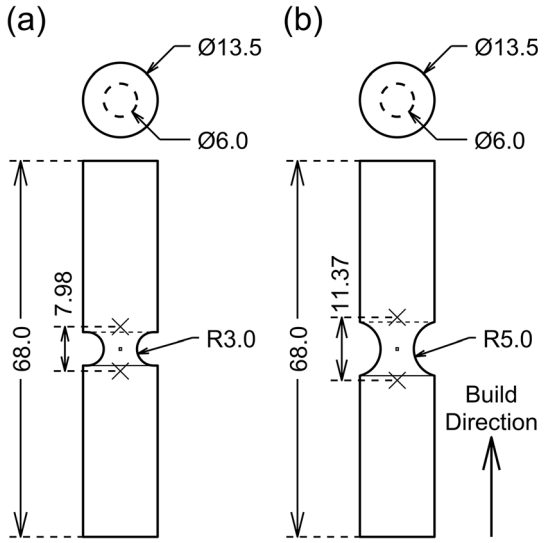

Fig. 1. Notched tension sample geometries: (**a**) R3NT and (**b**) R5NT. The samples were designed to be fully dense except for the designed internal pore schematically shown at the centers. The lengths of 7.98 and 11.37 represent the virtual extensometers used for the R3NT and R5NT geometries, respectively. The vertical build direction was along the axis of each sample.

pore was visible on the fracture surface (Fig. 2c) of all samples but one, which was not considered in the subsequent analysis. For a list of specimens, see Supplementary Table S-1 (refer to online Supplementary Material). Three nominally dense specimens of the R3NT and R5NT geometries were also tested.

To verify the samples were nearly fully dense apart from the designed internal pore, the densities were measured with the Archimedes method. Samples without designed pores had densities of 4.406 ± 0.006 g/cm^3, while the samples containing internal pores had densities of 4.402 ± 0.003 g/cm^3; all densities exceeded 99.3%.

X-ray Computed Tomography

To verify the pores were fabricated as designed, for each unique sample type, a single specimen was scanned with X-ray Computational Tomography (XCT) (v|tome|x L300 nano/microCT machine, General Electric, Boston, MA). Voxel edge lengths of 10.0 μm were used along with the same scanning settings used in a previous study on the same material.[20] Image segmentation was performed with Avizo 2020.2 (Thermo Fisher Scientific Inc., Waltham, MA).

The diameter, location, and aspect ratio of the pores were measured, and compared with the designed dimensions (Fig. 3). For pores intended to have equivalent diameters of 424 μm (0.25% cross-sectional area) and 600 μm (0.50% cross-sectional area), the mean measured equivalent

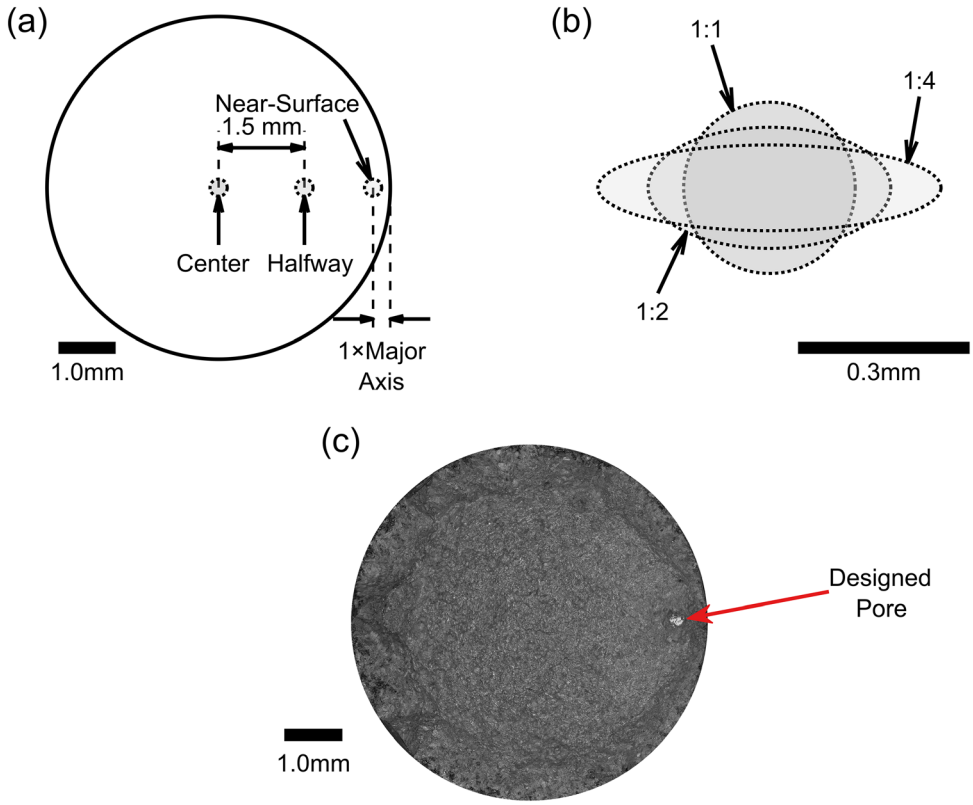

Fig. 2. Schematics of internal pore geometries. (a) Pores were located at either the center, middle, or near the surface, with the center of the pores located near the surface located one major axis away from the free surface. (b) The pores were designed to be elliptical, with aspect ratio between major and minor axes varying from 1:1 to 1:2 to 1:4. (c) Designed pores were clearly visible on the fracture surfaces as bright, reflective features, as shown in this representative optical fractograph.

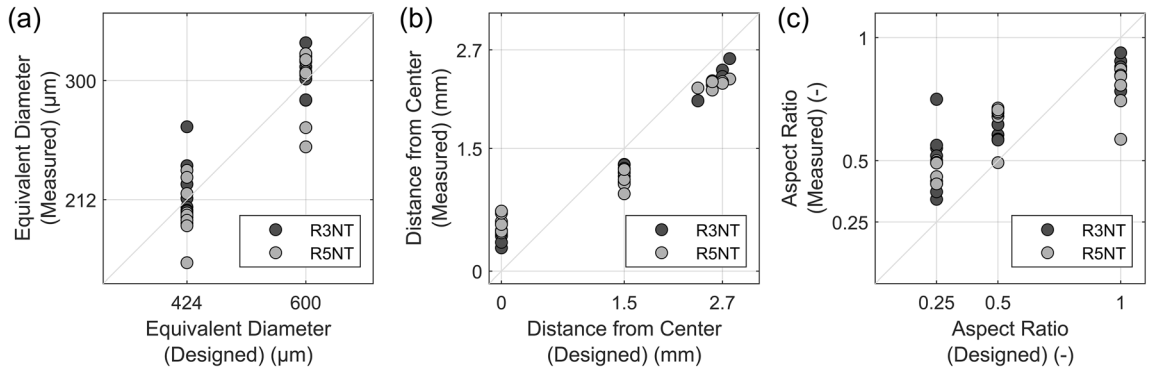

Fig. 3. Comparison between nominal and measured pore parameters, using X-ray computed tomography. (a) The equivalent diameter was approximately half of the designed value, (b) the centrally located pores were slightly off-center, while the other pores were closer to the center than designed, and (c) circular pores were less circular while elliptical pores were more circular than designed.

diameters were 210 μm (0.12% cross-sectional area) and 309 μm (0.27% cross-sectional area), respectively (Fig. 3a). The equivalent diameters were almost exactly half of the designed values. The variance, accounting for all aspect ratios and locations, was 22 μm for the smaller class of pores, and 26 μm the larger class. Therefore, the process produced pores of a repeatable size despite the size being consistently smaller than intended.

Pores intended to be centrally located were typically 0.5 mm off-center, while the near-surface pores were located closer to the sample's center than their intended locations (Fig. 3b). The discrepancy is due to a timing offset between the system

controlling the laser shutoff and the machine laser toolpath. Finally, there was small variance in aspect ratio (less than 0.05 in all cases), but pores intended to be circular typically had aspect ratios of 0.82 (Fig. 3c). The elongated pores with an intended aspect ratio of 0.25 had an average aspect ratio of 0.49, and it is hypothesized that melt pool spreading eroded the minor diameter more significantly than the major diameter.

Mechanical Testing

Samples were subjected to quasistatic mechanical testing in tension to fracture using a universal testing machine (Criterion Model 45, MTS, Eden Prarie, MN) at a quasi-static crosshead displacement rate of 0.007 mm/s. Displacement was measured through stereographic digital image correlation (DIC); specimens were coated with white paint with a black spray-painted speckle pattern applied before testing. Virtual extensometers had lengths of 7.98 mm and 11.37 mm for R3NT and R5NT samples, respectively (Fig. 1).

J-Integral Simulations

J-integral simulations were conducted with finite element analysis (Abaqus, 2022, Dassault Systèmes, Vélizy-Villacoublay, France). The Begley-Landis method was adopted, where two finite element models were used: one with the nominal pore geometry, and another where the pore was uniformly dilated by a small increment, in this case 10 μm in all directions.[34] J at displacement x was calculated as:

$$J(x) = \left(\int_0^x \left(F_{pore} - F_{pore+\Delta pore}\right) d\delta\right)/\Delta A, \tag{4}$$

where F represents the forces in the finite element simulation, $d\delta$ is an increment of displacement, and ΔA is the difference in crack cross-sectional area between the two models. Unlike the contour integral approach, where J is locally obtained around the perimeter of the crack, the Begley-Landis method calculates a single J-integral that characterizes the entire pore. A calibrated anisotropic plasticity model developed for L-PBF Ti-6Al-4V was used in simulations.[35] The crack was modeled as a free surface with no initial height, and in the vicinity of the crack, the typical element edge length was 10 μm.

Ductile Fracture Models

The Mohr–Coulomb model assumes that failure occurs with a critical linear combination of shear and normal stress. Bai and Wierzbicki extended the failure criterion to ductile materials by reformulating it as a strain-formulated model through using an assumed plasticity model, where the critical strain, $\bar{\varepsilon}_f^{MMC}$, is:

$$\bar{\varepsilon}_f^{MMC} = \left(\frac{A}{c_2}\left[c_\theta^s + \frac{\sqrt{3}}{2-\sqrt{3}}\left(c_\theta^{ax} - c_\theta^s\right)\left(\sec\left(\frac{\bar{\theta}\pi}{6}\right) - 1\right)\right]\left[\sqrt{\frac{1+c_1^2}{3}}\cos\left(\frac{\bar{\theta}\pi}{6}\right) + c_1\left(\eta + \frac{1}{3}\sin\left(\frac{\bar{\theta}\pi}{6}\right)\right)\right]\right)^{-1/n} \tag{5}$$

$$c_\theta^{ax} = \begin{cases} 1 \; \bar{\theta} \geq 0 \\ c_\theta^c \; \bar{\theta} < 0 \end{cases} \tag{6}$$

where A is the strength coefficient and n is the strain hardening coefficient. The four parameters, c_1, c_2, $c_\theta{}^c$, and $c_\theta{}^s$, are calibration coefficients.[24]

The modified Mohr–Coulomb model (MMC) describes the failure strain for proportional loading. To account for non-proportional loading in mechanical testing, a damage parameter, D, is introduced. Damage is defined to be zero for virgin material, and failure occurs at a value of one. Damage linearly accumulates with an increment of equivalent plastic strain, depending on the weighting function in Eq. 5:

$$D = \int_0^{\varepsilon} \frac{1}{\bar{\varepsilon}_{MMC}^p} d\varepsilon^p \tag{7}$$

The mean stress triaxiality and normalized Lode angle parameters are defined as:

$$\eta_{mean} = \frac{1}{\bar{\varepsilon}_f^p}\int_0^{\bar{\varepsilon}_f^p} \eta d\varepsilon^p, \bar{\theta}_{mean} = \frac{1}{\bar{\varepsilon}_f^p}\int_0^{\bar{\varepsilon}_f^p} \bar{\theta} d\varepsilon^p \tag{8}$$

Two fracture surfaces were calibrated: one for smaller pores (0.12% of the cross-sectional area) and one for larger pores (0.25% of the cross-sectional area). Samples containing circular pores were used for calibration. Three calibration points were used for both the R3NT and R5NT geometries: one for pores located at the center of the samples, another for pores near the surface of samples, and the last for pores located halfway between the center and surface. The stress states were obtained from material points located at the center position of each pore in the corresponding dense finite element models. The mean stress state for each sample is shown in Fig. 4a. When the pore was located at the center of the sample, an axisymmetric stress state was probed, while off-center pores probed other stress states.

An additional calibration point at negative normalized Lode angle parameter was required to calibrate the fracture models. Fully dense equibiaxial punch samples from a previous study on Ti-6Al-4V[36] were used; the equibiaxial tension stress state was considered to be an anchor point, because with that sample's geometry, LOF pores oriented along the build direction would be compressed and therefore would not reduce the strain to failure.[31] The

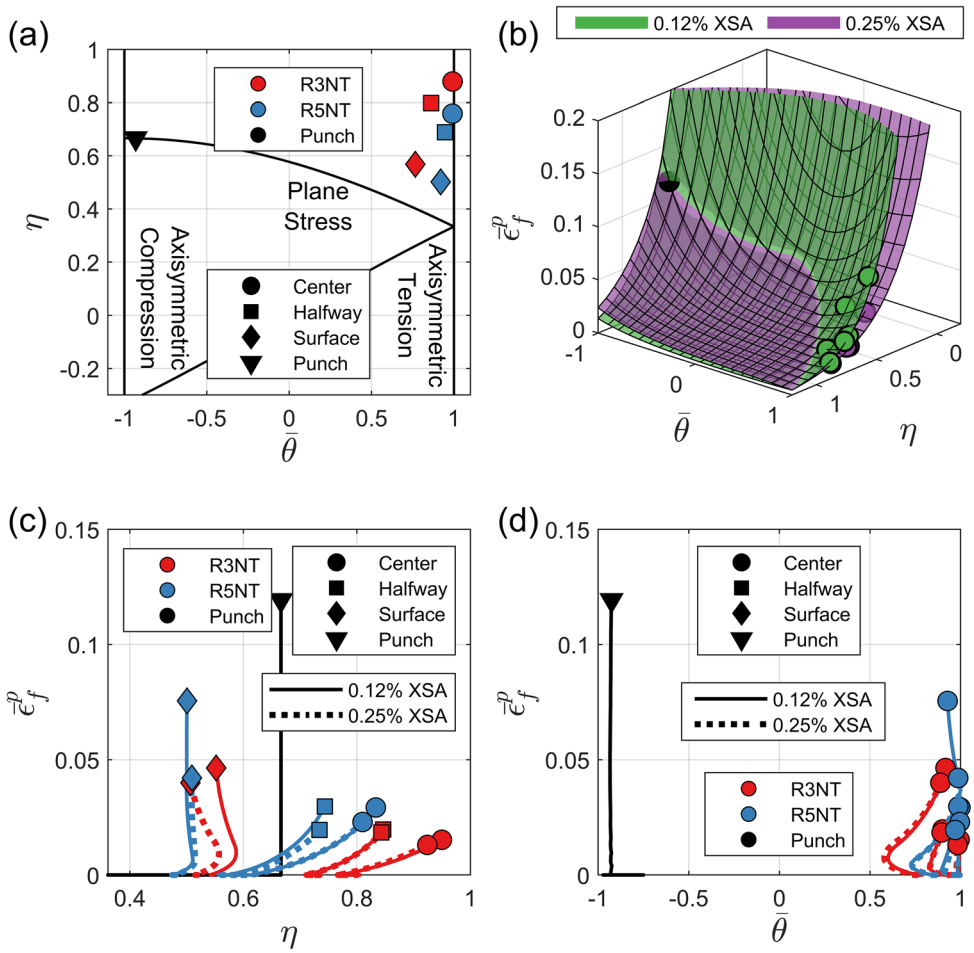

Fig. 4. (a) Mean stress state at the location of the center of the pore. The two *vertical lines* represent axisymmetric tension and compression stress states, and the *curve* at intermediate normalized Lode angle parameters represents plane stress states.[24] (b) Calibrated MMC fracture surfaces for samples containing pores of 0.12% and 0.25% of the cross-sectional area. Plastic equivalent strain as a function of (c) mean stress triaxiality and (d) mean normalized Lode angle parameter.

fracture surfaces were calibrated by using a multivariable nonlinear optimizer (*fmincon*, MATLAB R2020b, The MathWorks, Inc., Natick, MA) to reduce the difference between damage at failure and unity. The calibrated coefficients are presented in Table I.

EXPERIMENTAL RESULTS AND DISCUSSION

Mechanical Testing

The displacement to failure for each sample is shown in Fig. 5. For the higher stress triaxiality R3NT samples (Fig. 5a), the displacement to failure consistently fell between 0.15 mm and 0.18 mm with the exception of samples containing small pores (0.12% cross-sectional area) located near the surface, which failed between 0.19 mm and 0.21 mm. Likewise, for the lower stress triaxiality R5NT samples (Fig. 5b), small pores located near the surface fractured at large displacements, between 0.27 mm and 0.31 mm. All other R5NT samples failed between displacements of 0.17 mm and 0.22 mm. The R3NT and R5NT dense samples fractured with displacements between 0.25 ± 0.01 mm and 0.30 ± 0.02 mm, respectively. See Supplementary Table S-2 for the maximum force and displacement to failure for each type of sample and pore configuration.

To determine which pore features dominated the failure behavior (size, location, or aspect ratio), an analysis of variance (ANOVA) analysis was conducted, with the pore characteristics as the categorical factors and the displacement to failure being the response variable. In addition to the main effects of pore size, location, and aspect ratio, two-factor interactions were analyzed, which quantify any additional change in displacement to failure due to simultaneous change of two categorical factors. A critical significance value of $\alpha = 0.05$ was used to select pore features and interactions to study further with modeling. The statistical

Table I. Modified Mohr Coulomb fracture model calibration coefficients

Pore size	c_1 [-]	c_2 [MPa]	c_θ^s [-]	c_θ^c [-]
0.12% cross-sectional area	0.108	700	0.926	1.02
0.25% cross-sectional area	0.078	654	0.887	0.975

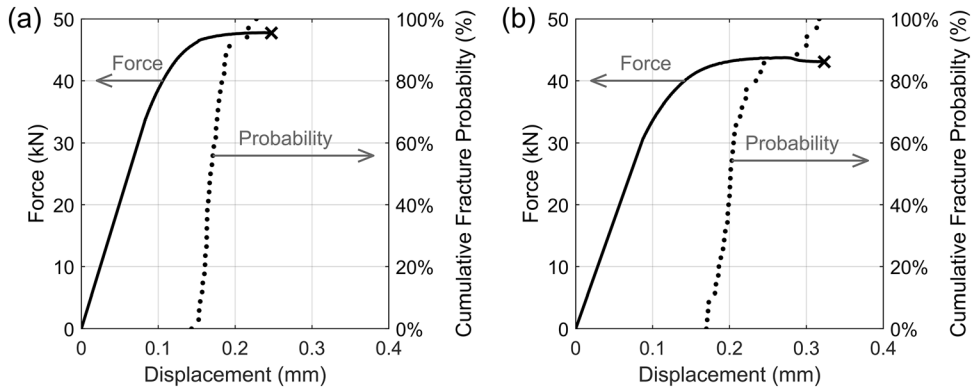

Fig. 5. Force–displacement curves for dense (a) R3 and (b) R5 samples along with cumulative distribution functions of the displacement to failure for samples containing pores. The samples containing internal pores failed at smaller displacements than the dense samples, verifying that the pores dominated the fracture behavior.

significance of the parameters is shown in Fig. 6, *where the F-test compares the ratio of variance of displacement to failure between different pore parameters with the in-group variance; see Supplementary Table S-3 for ANOVA analysis details. The large F-values of the pore size and location show that larger pores and pores located near the sample's center decrease the displacement to failure in a statistically significant manner. The statistically significant interaction term between pore size and location shows that the displacement to failure is more sensitive to location for samples containing small pores as opposed to large pores (visually shown in Fig. 7). For both geometries, the aspect ratio was neither significant as a main effect nor as an interaction, and therefore any effect of the aspect ratio on the displacement to failure cannot be isolated from experimental noise.*

J-Integral Results

The J-integral was measured as a function of displacement for the various pore geometries (Fig. 8). Nearly all samples failed at a critical J-integral (J_f) of 23 ± 4 kN, and J_f was at the lower range of that reported for hot isostatically pressed electron-beam Ti-6Al-4V (23–184 kN/m), due to HIP coarsening the microstructural features.[37,38]

For the R3NT geometry, J reached a critical value of 23 kN/m between a displacement of 0.16 mm and 0.19 mm for all geometries with the exception of samples containing small pores (0.12% cross-sectional area), where J_f of 23 kN/m corresponded to a displacement of 0.23 mm. At small displacements, strains were largest near the surface, and therefore J was largest for pores close to the surface (Fig. 8c). As the full cross-section yielded, the strain redistributed, with greater strain accumulation near the center, and correspondingly the crack driving force was larger near the center (Fig. 8e). The critical pore location shifted from near the surface to the sample's center with increasing deformation. In high-cycle fatigue tests, for which displacements are small, failure is typically due to near-surface defects, whereas in fully monotonic loading experiments, pores located near the surface are most benign.[10,39,40]

The R5NT samples behaved similarly to the R3NT samples. J was initially smaller for samples containing pores located at the center (Fig. 8d), and J of pores at the center superseded J of pores near the surface at larger displacements (Fig. 8e).

J for samples containing elliptical pores (1:4 aspect ratio) was compared with J of samples containing circular pores (Fig. 8c–f). When the pore location and size were the same, the elliptical pores typically had a higher J-integral than the circular pore. However, the difference was small (less than 10% at a given displacement) and its effect is less

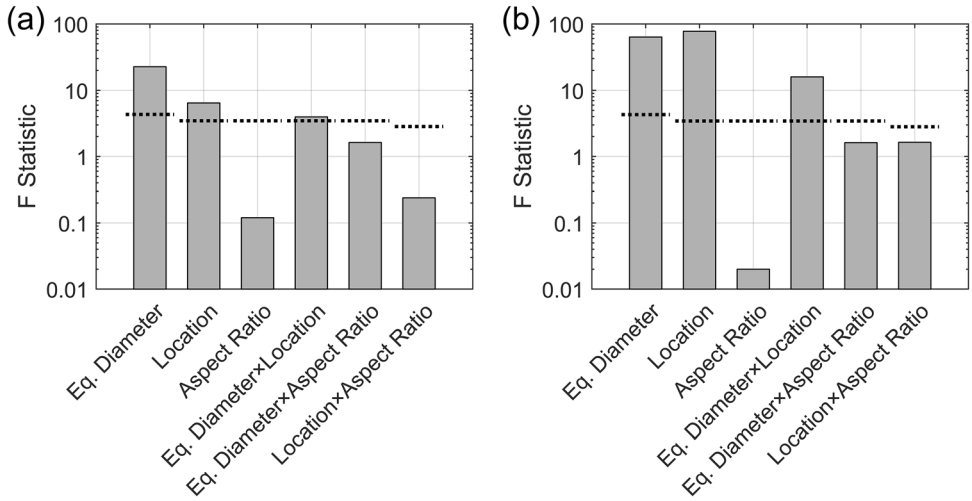

Fig. 6. *F*-values of ANOVA analysis on displacement to failure of (a) R3NT and (b) R5NT geometries. The main effects are equivalent diameter, location, and aspect ratio, and their two-factor interactions are represented with " × " symbols. The degrees of freedom vary for different effects, and therefore for a significance level of $\alpha = 0.05$, the critical value of F ranges between 2.8 and 4.3. For both sample geometries, the equivalent pore diameter and pore location were found to be critical, as well as the interaction between equivalent diameter and location.

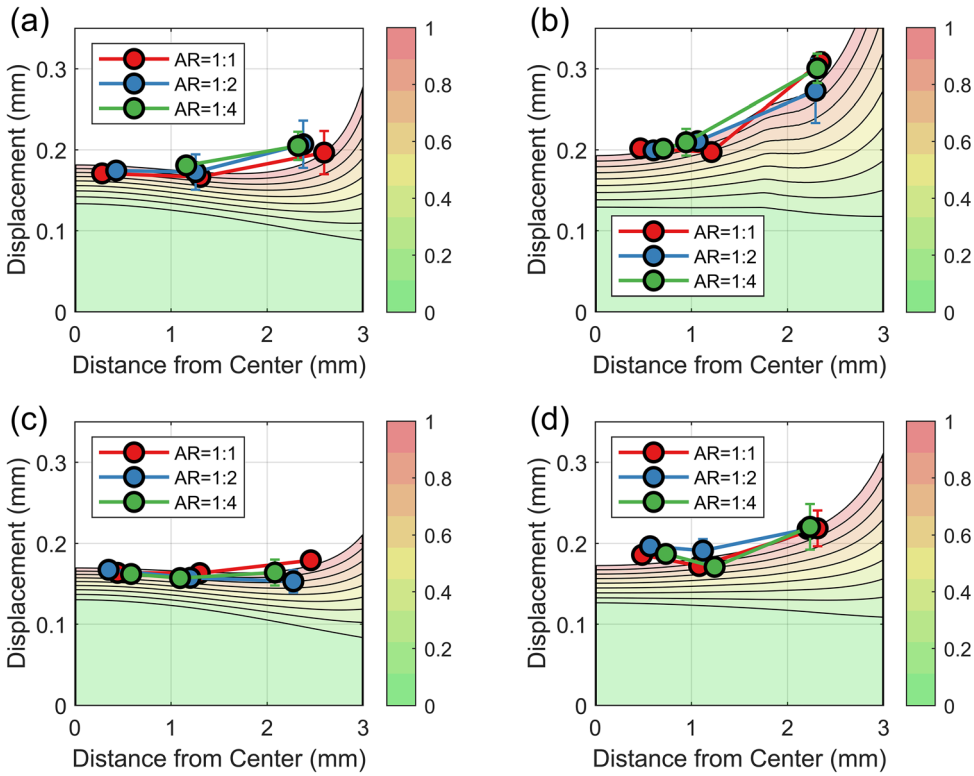

Fig. 7. Contours of damage accumulation for 0.12% cross-sectional area pores for (a) R3NT and (b) R5NT geometries, and for 0.25% cross-sectional area pores for (c) R3NT and (d) R5NT geometries. Displacements to failure (mean plotted with *error bars* indicating standard deviation) as a function of pore distance from the center are superimposed. The *error bars* show the standard error between the two experimentally measured displacements to failure.

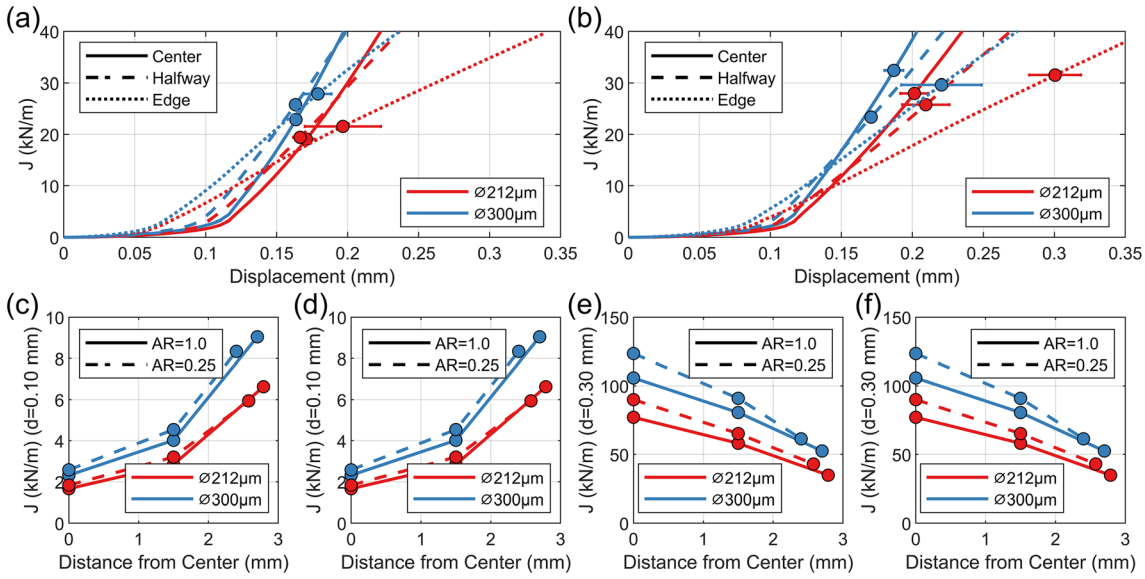

Fig. 8. Simulated J-integral versus displacement for pores occupying 0.12% and 0.25% of cross-sectional area, with an aspect ratio of 1:1, and in the center, middle, or near surface within (a) R3NT and (b) R5NT samples. *Symbols* represent the experimentally measured displacements to failure. At small applied displacements (shown here for 0.10 mm), the crack driving force is highest near the sample surface for both (c) R3NT and (d) R5NT geometries, where the plastic strain accumulation is highest. Conversely, at larger displacements (shown here for 0.30 mm) for the (e) R3NT and (f) R5NT geometries, as plastic strain accumulates more quickly in the center of the sample with applied displacement, the crack driving force is highest in the center.

significant than either pore location or size. Additionally, the pores were not as elliptical as designed (Fig. 3c). Therefore, although the J-integral analysis suggests that elliptical pores should have caused fracture at smaller displacements than circular pores, the difference was insufficient to be experimentally detectable.

This study's conclusions may be extended to anticipate what would occur if the material's toughness, J_f, were modified without significantly modifying other properties. For a tougher material with an increased J_f, only minimal increase in ductility would be observed due to the steep slope of J with respect to displacement for pores located at the center. However, if a specimen only contained pores near the surface, there would be a large increase in displacement to failure. Conversely, a less tough material with lower J_f would be more equally susceptible to fracture due to either surface or centrally located flaws.

Ductile Fracture Models

The MMC model's damage accumulation with respect to location is compared with the experimentally measured displacements to failure in Fig. 7. See Supplementary Table S-2 for the mean stress state and plastic equivalent strain at fracture for each sample type and pore configuration. For the R3NT geometry, whether for small pores (0.12% of the cross-sectional area) (Fig. 7a) or for larger pores (0.25% of the cross-sectional area) (Fig. 7c), damage accumulation began at smaller displacements for material points near the surface. However, once material points near the sample's center began accumulating damage, the damage increased faster than at the outside. The increased damage accumulation at the center can be attributed to the stress triaxiality being largest at that location (Fig. 4c). Locations near the surface had smaller normalized Lode angle parameters than those near the center (Fig. 4d), which alone increased the rate of damage accumulation; however, this effect was offset by the increased stress triaxiality near the center. There was little difference in either stress triaxiality or normalized Lode angle parameter (Fig. 4c, d) between the sample's center and halfway to the surface, and therefore the rate of damage accumulation was nearly constant for material points between these two locations.

For the R5NT geometry, damage began accumulating simultaneously across the entire sample (Fig. 7b, d). The decreased stress triaxiality towards the sample's surface resulted in a decreased rate of damage accumulation, and this effect was more pronounced than for the R3NT geometry. The relative magnitudes are consistent with the experimental results, for which the ANOVA analysis shows that the pore's location is more significant for the R5NT samples than for the R3NT samples (Fig. 6).

Although the ductile fracture model was calibrated only for circular pores, the aspect ratio had little effect on the displacement to failure, and therefore the ductile fracture model is also applicable to samples with elliptical pores.

CONCLUSION

In this study, notched tension samples, each containing a single designed internal pore, with size, location, and aspect ratio varying among samples, were produced using L-PBF and subjected to tensile loading. The study's primary conclusions are:

- Even at only 0.12–0.25% of the cross-sectional area, the internal pores caused nearly all samples to fail earlier than fully dense samples. ANOVA analysis, with a response variable of the displacement to failure, identified that the two most significant pore features were size and location, while aspect ratio was not significant compared with noise. On average, pores located near the center of the samples caused fracture at a displacement 19% smaller than for samples with a pore located near the surface; and samples containing a larger flaw (0.25% of the cross-sectional area) fractured at a displacement 15% smaller than for samples containing smaller pores (0.12% of the cross-sectional area).
- The samples fractured at a critical J-integral of approximately 23 kN/m, which is within the range of the 23–184 kN/m reported from J-integral tests conducted on additively manufactured Ti-6Al-4V, where the highest values in this range correspond to samples that had been hot isostatically pressed.
- At small displacements, both the J-integral analysis and the MMC fracture model's damage accumulation rate were largest for pores located near the sample's surface, while at large displacements, centrally located pores were most critical.

SUPPLEMENTARY INFORMATION

The online version contains supplementary material available at https://doi.org/10.1007/s11837-023-05751-4.

ACKNOWLEDGEMENTS

The financial support provided by the National Science Foundation through award number CMMI-1652575 and the National Science Foundation Graduate Research Fellowship under Grant No. DGE1255832 is gratefully acknowledged. The authors are grateful to Abdalla Nassar at Penn State's Center for Innovative Materials Processing through Direct Digital Deposition (CIMP-3D) for his support in the manufacturing of the samples, and for Sophia Craparo's assistance with quantitative XCT analysis.

CONFLICT OF INTEREST

The authors declare that they have no conflicts of interest.

REFERENCES

1. A. Dareh Baghi, S. Nafisi, R. Hashemi, H. Ebendorff-Heidepriem, and R. Ghomashchi, *J. Manuf. Process.* 68, 1031 (2021).
2. Y. Chong, T. Bhattacharjee, J. Yi, A. Shibata, and N. Tsuji, *Scr. Mater.* 138, 66 (2017).
3. M. Seifi, A. Salem, J. Beuth, O. Harrysson, and J.J. Lewandowski, *JOM* 68, 747 (2016).
4. G. Lütjering and J. C. Williams, *Titanium*, 2nd ed. (Springer, Berlin/ Heidelberg, Germany, 2007).
5. M. Gorelik, *Int. J. Fatigue* 94, 168 (2017).
6. M. Seifi, M. Gorelik, J. Waller, N. Hrabe, N. Shamsaei, S. Daniewicz, and J.J. Lewandowski, *JOM* 69, 439 (2017).
7. Z. Snow, A.R. Nassar, and E.W. Reutzel, *Addit. Manuf.* 36, 101457 (2020).
8. M. Grasso and B. M. Colosimo, *Meas. Sci. Technol.* **28**, 1 (2017).
9. N. Sanaei, A. Fatemi, and N. Phan, *Mater. Des.* 182, 108091 (2019).
10. R. Biswal, X. Zhang, A.K. Syed, M. Awd, J. Ding, F. Walther, and S. Williams, *Int. J. Fatigue* 122, 208 (2019).
11. G. Kasperovich, J. Haubrich, J. Gussone, and G. Requena, *Mater. Des.* 105, 160 (2016).
12. P. Promoppatum, R. Srinivasan, S.S. Quek, S. Msolli, S. Shukla, N.S. Johan, S. van der Veen, and M.H. Jhon, *J. Mater. Process. Technol.* 300, 117426 (2022).
13. J.V. Gordon, S.P. Narra, R.W. Cunningham, H. Liu, H. Chen, R.M. Suter, J.L. Beuth, and A.D. Rollett, *Addit. Manuf.* 36, 101552 (2020).
14. S. Tammas-Williams, P.J. Withers, I. Todd, and P.B. Prangnell, *Scr. Mater.* 122, 72 (2016).
15. ISO/ASTM 52900 Standard, ASTM International **i**, 1 (2015).
16. Q. Luo, L. Yin, T.W. Simpson, and A.M. Beese, *Addit. Manuf.* 56, 102915 (2022).
17. T. Montalbano, B.N. Briggs, J.L. Waterman, S. Nimer, C. Peitsch, J. Sopcisak, D. Trigg, and S. Storck, *J. Mater. Process. Technol.* 294, 117113 (2021).
18. S. Chen and S. Osovski, *Mech. Mater.* 148, 103513 (2020).
19. R. Fadida, A. Shirizly, and D. Rittel, *Mech. Mater.* 147, 103413 (2020).
20. E.T. Furton, A.E. Wilson-Heid, and A.M. Beese, *Addit. Manuf.* 48, 102414 (2021).
21. A.E. Wilson-Heid, T.C. Novak, and A.M. Beese, *Exp. Mech.* 59, 793 (2019).
22. A.E. Wilson-Heid and A.M. Beese, *Addit. Manuf.* 39, 101862 (2021).
23. L.X. Meng, D.D. Ben, H.J. Yang, H.B. Ji, D.L. Lian, Y.K. Zhu, J. Chen, J.L. Yi, L. Wang, J.B. Yang, and Z.F. Zhang, *Mater. Sci. Eng., A* 815, 141254 (2021).
24. Y. Bai and T. Wierzbicki, *Int. J. Fract.* 161, 1 (2010).
25. Y. Bai, X. Teng, and T. Wierzbicki, *J. Eng. Mater. Technol.* 131, 021002 (2009).
26. T. Wierzbicki, Y. Bao, Y.W. Lee, and Y. Bai, *Int. J. Mech. Sci.* 47, 719 (2005).
27. H. Li, M.W. Fu, J. Lu, and H. Yang, *Int. J. Plast.* 27, 147 (2011).
28. H. Zhang, T. Gao, J. Chen, X. Li, H. Song, and G. Huang, *Materials* 15, 3429 (2022).
29. J.R. Rice and D.M. Tracey, *J. Mech. Phys. Solids* 17, 201 (1969).
30. P. W. Bridgman, *Studies in Large Plastic Flow and Fracture*, 1st ed. (Harvard University Press, Cambridge, MA, 1964).
31. A.E. Wilson-Heid, E.T. Furton, and A.M. Beese, *Materials* 14, 1 (2021).

32. X.K. Zhu and J.A. Joyce, *Eng. Fract. Mech.* 85, 1 (2012).
33. C.F. Shih, *J. Mech. Phys. Solids* 29, 305 (1981).
34. J.A. Begley and J.D. Landes, *Am. Soc. Test. Mater.* 514, 1 (1972).
35. A.E. Wilson-Heid, S. Qin, and A.M. Beese, *Mater. Sci. Eng., A* 738, 90 (2018).
36. A.E. Wilson-Heid and A.M. Beese, *Mater. Sci. Eng., A* 761, 137967 (2019).
37. E. Lucon, J. Benzing, and N. Hrabe, *Mater. Perform. Charact.* 9, 701 (2021).
38. M. Seifi, A. Salem, D. Satko, J. Shaffer, and J.J. Lewandowski, *Int. J. Fatigue* 94, 263 (2017).
39. Y.N. Hu, S.C. Wu, P.J. Withers, J. Zhang, H.Y.X. Bao, Y.N. Fu, and G.Z. Kang, *Mater. Des.* 192, 108708 (2020).
40. S. Tammas-Williams, P.J. Withers, I. Todd, and P.B. Prangnell, *Sci. Rep.* 7, 1 (2017).